# Remote sensing of cirrus cloud vertical size profile using MODIS data

Xingjuan Wang,[1] K. N. Liou,[1] Steve S. C. Ou,[1] G. G. Mace,[2] and M. Deng[3]

Received 20 October 2008; revised 10 February 2009; accepted 27 February 2009; published 6 May 2009.

[1] This paper describes an algorithm for inferring cirrus cloud top and cloud base effective particle sizes and cloud optical thickness from the Moderate Resolution Imaging Spectroradiometer (MODIS) 0.645, 1.64 and 2.13, and 3.75 $\mu$m band reflectances/radiances. This approach uses a successive minimization method based on a look-up library of precomputed reflectances/radiances from an adding-doubling radiative transfer program, subject to corrections for Rayleigh scattering at the 0.645 $\mu$m band, above-cloud water vapor absorption, and 3.75 $\mu$m thermal emission. The algorithmic accuracy and limitation of the retrieval method were investigated by synthetic retrievals subject to the instrument noise and the perturbation of input parameters. The retrieval algorithm was applied to three MODIS cirrus scenes over the Atmospheric Radiation Measurement Program's southern Great Plain site, north central China, and northeast Asia. The reliability of retrieved cloud optical thicknesses and mean effective particle sizes was evaluated by comparison with MODIS cloud products and qualitatively good correlations were obtained for all three cases, indicating that the performance of the vertical sizing algorithm is comparable with the MODIS retrieval program. Retrieved cloud top and cloud base ice crystal effective sizes were also compared with those derived from the collocated ground-based millimeter wavelength cloud radar for the first case and from the Cloud Profiling Radar onboard CloudSat for the other two cases. Differences between retrieved and radar-derived cloud properties are discussed in light of assumptions made in the collocation process and limitations in radar remote sensing characteristics.

**Citation:** Wang, X., K. N. Liou, S. S. C. Ou, G. G. Mace, and M. Deng (2009), Remote sensing of cirrus cloud vertical size profile using MODIS data, *J. Geophys. Res.*, *114*, D09205, doi:10.1029/2008JD011327.

## 1. Introduction

[2] Cirrus clouds are frequently finite in nature and display substantial horizontal variability [*Minnis et al.*, 1993; *Mishchenko et al.*, 1996]. On the basis of the time series of backscattering coefficients derived from lidar and radar returns [*Sassen*, 1991; *Spinhirne and Hart*, 1990; *Mace et al.*, 2002], cirrus clouds also show significant vertical inhomogeneity in terms of extinction coefficient and ice water content (IWC), and are strongly sensitive to vertical temperature distribution [*Ou and Liou*, 1995]. *Miloshevich and Heymsfield* [1997] and *Heymsfield and Iaquinta* [2000] analyzed in situ balloon-borne ice crystal replicator data, and showed that the variation of ice crystal size and shape distributions within midlatitude cirrus clouds tend to be stratified: small nonspherical or quasi-spherical ice crystals are predominant in the upper layer, pristine single ice crystals and bullet rosettes with well defined hexagonal shapes are prominent in the middle layer, and the bottom layer mainly contains larger but irregularly shaped aggregates formed by collision and sublimation processes of ice crystals. Moreover, the mean cloud particle size increases from cloud top downward, but sharply decreases to near-zero value at cloud base.

[3] The inhomogeneity of cirrus cloud composition has been shown to cause the spatial variation of atmospheric radiative heating/cooling rates. *Gu and Liou* [2001, 2006] and *Gu et al.* [2003] used the Fu-Liou radiative transfer model [*Fu and Liou*, 1993; *Fu*, 1996] incorporated into the University of California at Los Angeles general circulation model to demonstrate that the vertical profile of ice crystal mean effective size ($D_e$) drives the radiative heating/cooling rate profiles within cirrus clouds and surrounding cloudless areas, and concluded that this radiative effect due to the inhomogeneous cirrus cloud properties must be considered in the study of radiation/climate feedback. Obviously, a comprehensive knowledge of the spatial distribution of $D_e$ will improve the representation of cirrus clouds in weather and climate models.

[4] Limited vertical profiles of ice crystal size and shape distributions have been derived from in situ observations [*Miloshevich and Heymsfield*, 1997; *Kinne et al.*, 1997; G. McFarquhar et al., Horizontal and vertical profiles of in situ cloud properties measured during tropical warm pool international cloud experiment, paper presented at Sixteenth Atmospheric Radiation Measurement Science Team Meeting, Dep. of Energy, Atmos. Radiat. Meas. Program, Albuquerque,

[1]Department of Atmospheric and Oceanic Sciences, University of California, Los Angeles, Los Angeles, California, USA.
[2]Department of Meteorology, University of Utah, Salt Lake City, Utah, USA.
[3]Department of Atmospheric Science, University of Wyoming, Laramie, Wyoming, USA.


0148-0227/09/2008JD011327

New Mexico, 2006]. Retrieval techniques for the inference of the vertical profile of cloud microphysics and optical parameters from ground-based lidar and radar measurements have also been developed [*Sassen*, 1991; *Spinhirne and Hart*, 1990; *Matrosov et al.*, 1994; *Mace et al.*, 2002; *Comstock et al.*, 2002], but the development of retrieval methodology based on satellite imager data is still in its embryonic stage. *Liou et al.* [2002] combined collocated ground-based lidar/radar measurements and Advance Very High Resolution Radiometers (AVHRR) observations over the Atmospheric Radiation Measurement (ARM) Program's Southern Great Plain (SGP) site to construct three-dimensional (3-D) cirrus cloud parameter fields. Although this approach is capable of producing detailed 3-D cloud maps, its applicability is restricted both in time and space because of the limited access of collocated satellite and radar/lidar observations. By using a generalized parameterization of the vertical $D_e$ profile involving temperature from sounding/analysis, *Liou et al.* [2006] further developed a satellite remote sensing technique to produce 3-D IWC and $D_e$ fields of cirrus clouds for global application.

[5] Recently, the addition of CloudSat and Cloud Aerosol Lidar and Infrared Pathfinder Satellite Observations (CALIPSO) to the NASA's A-Train satellite constellation in 2006 has enabled the global mapping of cross sections of cirrus cloud properties, but the geographical coverage of the Cloud Profiling Radar (CPR) onboard CloudSat and the Cloud-Aerosol Lidar with Orthogonal Polarization (CALIOP) onboard CALIPSO is still limited to the suborbital track. Because of the wide cross-track scanning swath ($\sim$1300 km), and the excellent spatial resolution ($\sim$0.5 km for visible bands and 1 km for the rest of bands) of the Moderate Resolution Imaging Spectroradiometer (MODIS), a good alternative for global cirrus cloud vertical sizing over much larger areas is to develop a retrieval scheme to infer cirrus cloud vertical size profiles based on differences in the spectral reflection/absorption characteristics of MODIS near-infrared (IR) bands.

[6] The current MODIS cloud retrieval algorithm simultaneously retrieves the total cloud optical thickness ($\tau_c$) and a vertically averaged mean effective radius ($r_e$) using observed solar reflectances/radiances at one visible and three near-IR window bands [*King et al.*, 1997], assuming a plane-parallel cloud geometry with a vertically homogeneous composition. It is based on the physical principle that reflectances at nonabsorbing (for cloud particles) visible and absorbing near-IR wavelengths primarily depend on $\tau_c$ and $r_e$, respectively. Although this approach is straightforward and elegant, it cannot resolve the vertical structure of cirrus clouds because of the assumption of vertically homogeneous cloud composition. Consequently, for any cloudy pixel, the $r_e$ values inferred from individual near-IR bands are different from each other [*Baum et al.*, 2000]. *Platnick* [2000] explained these differences in retrieved water cloud $r_e$ by theorizing that the difference in the maximum photon penetration levels for individual near-IR bands causes the reflectance of stronger-absorbing bands to be primarily sensitive to cloud top properties, and the reflectance of weaker-absorbing bands to carry more information about the cloud's deeper structure. On the basis of this theory, *Chang and Li* [2002] used three MODIS near-IR band reflectances to infer the vertically linear profile of $r_e$ in low-level nonprecipitating stratus clouds. They assessed the performance of the retrieval method by comparison with in situ observation of microphysical profiles, and showed that the retrieved linear $r_e$ profiles are capable of capturing the vertical trend of variation in $r_e$. It appears that we can utilize the information content of MODIS visible and near-IR band reflectances/radiances to infer the vertical profile of ice crystal $D_e$ on the pixel level, on the basis of the unique characteristics of the difference in cloud absorption strength among these bands.

[7] This paper describes a cirrus cloud vertical sizing algorithm for inferring cloud top and cloud base effective sizes ($D_t$, $D_b$) and $\tau_c$ from the MODIS 0.645, 1.64, 2.13 and 3.75 $\mu$m band reflectances/radiances, using a successive minimization method based on a look-up library of precomputed reflectances/radiances from an adding-doubling radiative transfer program, subject to corrections for Rayleigh scattering at the 0.645 $\mu$m band, above-cloud water vapor absorption, and 3.75 $\mu$m thermal emission. The algorithmic accuracy and limitation of the retrieval method were investigated by synthetic retrievals subject to instrument noise and perturbation of input parameters.

[8] The retrieval algorithm was applied to three MODIS cirrus scenes over the Atmospheric Radiation Measurement Program's Southern Great Plain site, north central China, and northeast Asia. The reliability of retrieved cloud optical thicknesses and mean effective sizes was evaluated by comparisons with MODIS cloud products for all three cases, and retrieved cloud top and cloud base ice crystal effective sizes were compared with those derived from the ground-based millimeter wavelength cloud radar (MMCR) data for the first case, and from CPR/CloudSat data for the other two cases.

[9] The arrangement of the paper is as follows. Section 2 describes the retrieval methodology and forward radiative transfer modeling subject to various atmospheric and surface correction schemes. Section 3 contains description of error budget studies by performing synthetic retrievals and discussions of the algorithmic errors and retrieval errors caused by uncertainties in input parameters and instrument noises. Section 4 presents results of application of the vertical sizing algorithm to the three selected midlatitude MODIS scenes containing widespread stratiform cirrus clouds, their comparison with MODIS cloud products, and the assessment of retrieval performance using data from ground-based MMCR and space-based CloudSat/CPR. Last, a summary is given in section 5.

## 2. Theoretical Description of the Retrieval Approach

### 2.1. Retrieval Algorithm

[10] We developed a cirrus cloud vertical sizing algorithm to simultaneously retrieve $D_t$, $D_b$ and $\tau_c$, from the reflectance/radiance of MODIS visible 0.645 $\mu$m and near-IR 1.64, 2.13 and 3.75 $\mu$m bands, where $D_t$ and $D_b$ are defined as

$$D_{t,b} = (3/2) \cdot \left[ \sum_{h=1}^{M} \int_{L_{\min}}^{L_{\max}} V_h(L) n_{t,b}(h,L) dL \Big/ \sum_{h=1}^{M} \int_{L_{\min}}^{L_{\max}} A_h(L) n_{t,b}(h,L) dL \right]. \quad (1)$$

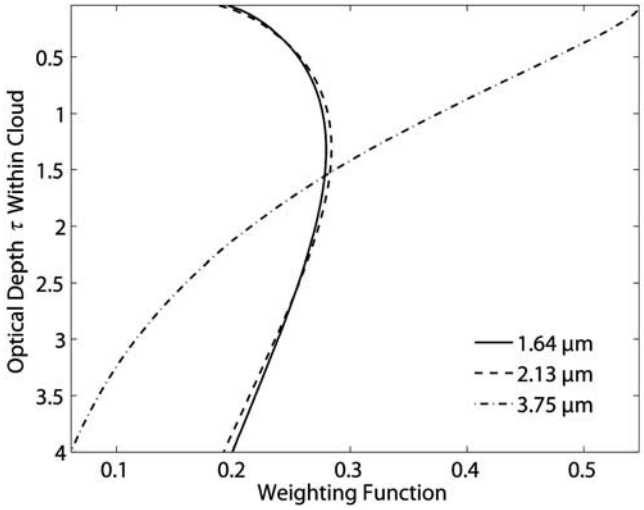


**Figure 1.** Weighting functions are calculated at MODIS 1.64, 2.13, and 3.75 $\mu$m bands for a cirrus cloud with $D_e$ = 40 $\mu$m and $\tau_c$ = 4.

$A_h(L)$ and $V_h(L)$ are the projected area and volume of the particle with habit index $h$ and maximum dimension $L$, respectively, and $n_t(h, L)$ and $n_b(h, L)$ are ice crystal size and shape distributions at cloud top and base, respectively.

[11] The retrieval algorithm uses a novel look-up table approach for the simultaneous retrieval of $D_t$, $D_b$ and $\tau_c$. To illustrate the relative contribution from different layers within the cloud to the total reflectance/radiance at the top of atmosphere, Figure 1 shows weighting functions for all three near-IR bands of a model cirrus cloud with $\tau_c$ = 4 and $D_e$ = 40 $\mu$m. These weighting functions are defined as $[dR(\tau)/d\tau]/R(\tau_c)$, and were obtained on the basis of the maximum photon penetration principle [*Platnick*, 2000]. Because of the stronger ice absorption in the 3.75 $\mu$m band, its weighting function peaks at a higher level than other weighting functions, implying that the 3.75 $\mu$m reflectance/radiance is more sensitive to cloud top properties. On the other hand, the weighting functions for 1.64 and 2.13 $\mu$m bands are almost identical, forming practically only one piece of information. Therefore, in the retrieval algorithm, the vertical profile of $D_e$ is constrained as a linear function of $\tau$, because there are essentially only two independent pieces of information available, which can only be used to retrieve the two sizes $D_t$ and $D_b$.

[12] The retrieval algorithm follows the numerical iterative approach to search for the converged solution of $D_t$, $D_b$, and $\tau_c$ that are associated with minimal differences between simulated and observed reflectance/radiance for all four bands. Figure 2 shows the flowchart for retrieving $D_t$, $D_b$, and $\tau_c$. First of all, the adding-doubling radiative transfer model is used to build a library of cloud-only radiative parameters for all combinations of reference values of $D_t$, $D_b$, and $\tau_c$. For each pixel identified as cirrus cloud, reflectance/radiance at the four bands and viewing geometry data are extracted from MODIS L1B products. Required input parameters, including cloud top temperature ($T_c$), cloud top pressure ($P_c$), surface albedos ($A_g$), and surface temperature ($T_g$) are extracted from MODIS data products. A comprehensive set of cloud-only reflectances/radiances for combinations of reference $D_t$, $D_b$, and $\tau_c$ are first computed and tabulated. Various pixel-dependent correction schemes are then applied and a look-up library of total reflectance/radiance for this particular pixel is built for the retrieval of cloud parameters for a cloudy pixel.

[13] The numerical iterative search program uses a successive minimization method. It starts by prescribing initial values of $D_t$ and $D_b$, then it retrieves and updates $\tau_c$ on the basis of the minimization of the 0.645 $\mu$m reflectance residual, retrieves and updates $D_t$ by minimizing the 3.75 $\mu$m radiance residual assuming updated value of $\tau_c$ and $D_b$, and lastly retrieves $D_b$ by minimizing 1.64 and/or 2.13 $\mu$m reflectance residual assuming updated $\tau_c$ and $D_t$ values. If all of the most updated $D_t$, $D_b$, and $\tau_c$ values differ from their respective values from the previous iteration by less than prescribed thresholds, or the number of iterative steps reaches a prescribed limit, the numerical procedure terminates, and the last set of $D_t$, $D_b$, and $\tau_c$ values is the retrieval solution. Otherwise, the iteration continues until they converge. The iteration is quite effective and usually takes only three to four steps to reach convergence.

### 2.2. Formulation and Modeling of Radiative Transfer

[14] For any given cirrus cloudy pixel identified by the MODIS Cloud/Phase Mask programs, the retrieval algorithm uses a look-up library of reflectance/radiance at the four spectral bands to retrieve $D_t$, $D_b$, and $\tau_c$. The generation of the look-up library is based on the ice crystal size and habit distribution models developed by *Baum et al.* [2005a]. These models were based on 1100 in situ measurements of ice crystal size and habit distributions obtained during several cirrus cloud field campaigns, including FIRE-I, FIRE-II, ARM Cloud IOP, CEPEX, and CRYSTAL-FACE, and were the most comprehensive size and habit distribution models currently available for application to the satellite remote sensing of cirrus clouds. Therefore, we expect that these models should represent ice crystal size and habit distributions for a variety of cirrus clouds observed by MODIS. Each ice crystal size distribution was fitted to the Gamma function, and parameters of the Gamma function were obtained by minimizing the difference between computed and measured IWC and median mass diameter. Both reference $D_t$ and $D_b$ vary from 10 to 180 $\mu$m with an interval of 10 $\mu$m. A composite ice crystal size distribution was obtained for each size bin based on fitted Gamma function parameters.

[15] The prescribed ice crystal habit distribution model varies with the maximum dimension ($L$). For $L < 60$ $\mu$m, these small particles are composed of 100% droxtals. For $60 < L < 1000$ $\mu$m, a mixture of 15% 3-D bullet rosettes, 50% solid columns, and 35% plates is prescribed. For $1000 < L < 2500$ $\mu$m, a mixture of 45% hollow columns, 45% solid columns, and 10% aggregates is prescribed. Finally, for $2500 < L < 9500$ $\mu$m, these large particles are composed of 97% 3-D bullet rosettes and 3% aggregates.

[16] The bulk single-scattering properties associated with each reference $D_t$ and $D_b$ were based on archived single-scattering properties for individual wavelength, $L$, and habit, which were computed by using the Finite difference Time Domain method and modified Geometric Optics method [*Yang et al.*, 2000; *Baum et al.*, 2005b]. The prescribed reference $\tau_c$ values are 0, 0.5, 1, 2, 4, 8, 16, and 32. Thus, for each spectral band and for a particular set of sun sensor

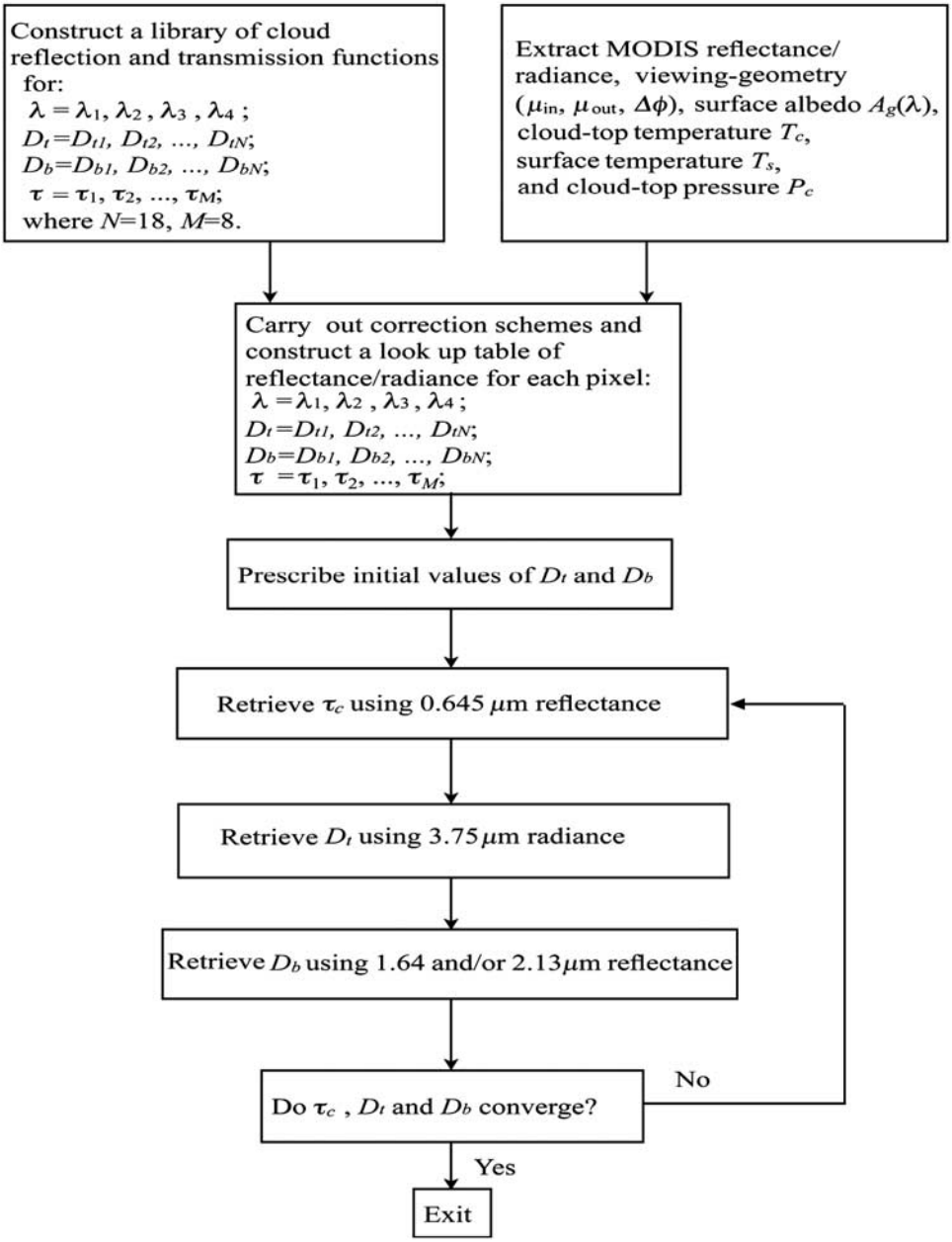


**Figure 2.** Flowchart of the retrieval algorithm.

geometry, the dimension of the look-up library is $18(D_t) \times 18(D_b) \times 8(\tau_c)$. For potential global application, the look-up library will have to be expanded to include the functional dependence of reflectances on the combination of reference solar and viewing zenith angles and relative azimuthal angle.

[17] We used an adding-doubling radiative transfer code specifically designed for simulating the radiative transfer in cirrus clouds. The adding-doubling method has been recognized as a very powerful tool for multiple-scattering calculations, particularly with reference to remote sensing applications [*Liou*, 2002]. For each combination of $D_t$, $D_b$ and $\tau_c$, the adding-doubling radiative transfer model was used to calculate cloud-only radiative parameters, which include the bidirectional transmission functions ($T$, $T^*$), the reflection functions ($R$, $R^*$), the transmissions ($\gamma$, $\gamma^*$), the reflections ($r$, $r^*$), and the spherical albedo ($\bar{r}^*$). The latter three quantities are determined on the basis of the following formulae:

$$\gamma^{(*)}(\mu) = (1/\pi)\int_0^{2\pi}\int_0^1 T^{(*)}(\mu', \mu, \varphi - \varphi')\mu' d\mu' d\varphi' + e^{-\tau/\mu}, \quad (2)$$

$$r^{(*)}(\mu) = (1/\pi)\int_0^{2\pi}\int_0^1 R^{(*)}(\mu', \mu, \varphi - \varphi')\mu' d\mu' d\varphi', \quad (3)$$

and

$$\bar{r}^* = 2\int_0^1 r^*(\mu) d\mu, \quad (4)$$

where $\mu$ and $\mu'$ are cosines of zenith angles for the outgoing and incoming directions, respectively. The superscript asterisk denotes the property related to the incident radiation at cloud base. The $\mu$ values are discretized into 8 Radau quadrature nodes within the interval (0,1], and the relative azimuthal angle between the sun and the sensor ($\Delta\varphi$) ranges between 0° to 180° with an interval of 30°. For prescribed sun sensor geometry, simulated cloud-only properties ($T$, $T^*$, $R$, $R^*$, $r$, $r^*$, $\gamma$ and $\gamma^*$) are calculated through linear interpolation between reference directions. Spherical albedo ($\bar{r}^*$) is not affected by viewing geometry and does not require interpolation.

[18] The observed total reflectance consists of cloud-only reflectance and the multiple reflection between surface and clouds [*Nakajima and Nakajima*, 1995]

$$R(\mu,\mu_0,\Delta\varphi) = R_c(\mu,\mu_0,\Delta\varphi) + \left[A_g/\left(1-\bar{r}^*A_g\right)\right]\gamma^*(\mu)\gamma(\mu_0). \tag{5}$$

In this study, surface albedo ($A_g$) data for the 0.645, 1.64 and 2.13 $\mu$m bands are compiled from the MODIS 16 day L3 1 km Global Albedo data product MOD43B3, and the 3.75 $\mu$m albedo is estimated from the MODIS 8 day L3 global surface temperature/emissivity data product MOD11C2. Thus, variation in the surface albedo has been accounted for, and retrieval errors due to uncertainties in the surface albedo have been minimized.

### 2.3. Correction for Above-Cloud Water Vapor Absorption Effect

[19] Water vapor absorption above the cloud is accounted for by assuming the atmosphere above cloud is purely absorptive [*Platnick et al.*, 2003]. The water vapor corrected reflectance $R_w$ is approximated by the following equation:

$$R_w = RT_u(\mu)T_u(\mu_0), \tag{6}$$

where $T_u(\mu_0)$ and $T_u(\mu)$ are transmittances in the solar incident and satellite viewing directions, respectively. The transmittance $T_u(\mu)$ is expressed as

$$T_u(\mu) = e^{-\tau_w(P_c)/\mu}, \tag{7}$$

where $\tau_w(P_c)$ is the water vapor absorption optical thickness for air mass above the cloud top pressure $P_c$. The optical thickness $\tau_w(P_c)$ is calculated from the correlated $k$ distribution method by assuming the water vapor profile in the U.S. Standard Atmosphere. A library of precomputed $\tau_w(P_c)$ is constructed.

### 2.4. Correction for Rayleigh Scattering Effect

[20] The Rayleigh scattering effect is more prominent in the 0.645 $\mu$m band than in the other three near-IR bands. *Wang and King* [1997] showed that neglecting Rayleigh scattering correction can cause a significant error in retrieved $\tau_c$ for large solar and/or viewing zenith angles. To account for the Rayleigh scattering above clouds, we adopted their Rayleigh-scattering parameterization scheme. The corrected bidirectional reflectance, $R_{0.645}$ is expressed as

$$\begin{aligned} R_{0.645}(\mu,\mu_0,\Delta\varphi) \cong & \left[\tau_r P^r(\mu,\mu_0,\Delta\varphi)\Big/ 4\mu\mu_0\right] \\ & + R_w(\mu,\mu_0,\Delta\varphi)e^{-\tau_r(1/\mu+1/\mu_0)} \\ & + (\tau_r/2\mu_0)r(\mu)e^{-\tau_r/\mu} + (\tau_r/2\mu)r(\mu_0)e^{-\tau_r/\mu_0}, \end{aligned} \tag{8}$$

where $P^r$ is the Rayleigh scattering phase function, $\tau_r$ is the Rayleigh optical thickness and can be calculated from $P_c$ [*Liou*, 2002]. The first and second terms on the right hand side account for the direct Rayleigh scattering without cloud reflection; and for the reflection of direct solar radiation by the cloud; respectively. The third and fourth terms are for the reflection of the direct solar radiation by the cloud subject to single scattering in the air; and for single scattering in the air subject to the reflection from the cloud, respectively.

### 2.5. Correction for Thermal Emission Contribution in the 3.75 $\mu$m Band

[21] For the 3.75 $\mu$m band, the thermal emission from both earth surface and cloud is a major component of the total measured radiance. The total radiance, $I_{3.75}$, can be approximated by the following equation [*Nakajima and Nakajima*, 1995]:

$$\begin{aligned} I_{3.75}(\mu,\mu_0,\Delta\varphi) = & R_w(\mu,\mu_0,\Delta\varphi)(\mu_0 F_0/\pi) \\ & + T_u(\mu)\left\{\gamma^*(\mu)\left[\left(1-A_g\right)/\left(1-\bar{r}^*A_g\right)\right]B(T_g)\right. \\ & \left. + [1-\gamma(\mu)-r(\mu)]B(T_c)\right\}, \end{aligned} \tag{9}$$

where $B$ is the Planck function, $F_0$ the extraterrestrial solar flux at 3.75 $\mu$m band, and $T_c$ and $T_g$ are cloud and surface temperatures, respectively. The first term on the right-hand side represents the reflected solar radiance, corrected for multiple reflection and water vapor absorption. The second term denotes the contribution from surface and cloud emissions attenuated by above-cloud water vapor absorption $T_u(\mu)$. For each cirrus cloudy pixel, the above corrections are applied to all combinations of reference $D_t$, $D_b$ and $\tau_c$, to create a look-up library of reflectance/radiance.

## 3. Error Budget Studies

### 3.1. Algorithmic Errors

[22] To assess the accuracy and limitations of the retrieval approach, we perform synthetic retrievals, using simulated reflectance/radiance in lieu of measurement data. For each of the three parameters, $D_t$, $D_b$, and $\tau_c$, we prescribed a set of intermediate values in between their neighboring library reference points. There are 17 intermediate $D_t$ and $D_b$ values ranging from 15 to 175 $\mu$m with an interval of 10 $\mu$m, and the following seven intermediate $\tau_c$ values: 0.25, 0.75, 1.5, 3, 6, 12, and 24. For each of the 2023 (= 17 × 17 × 7) combinations of the intermediate, $D_t$, $D_b$, and $\tau_c$ values, the simulated reflectance/radiance is determined from the adding-doubling radiative transfer program, using interpolated

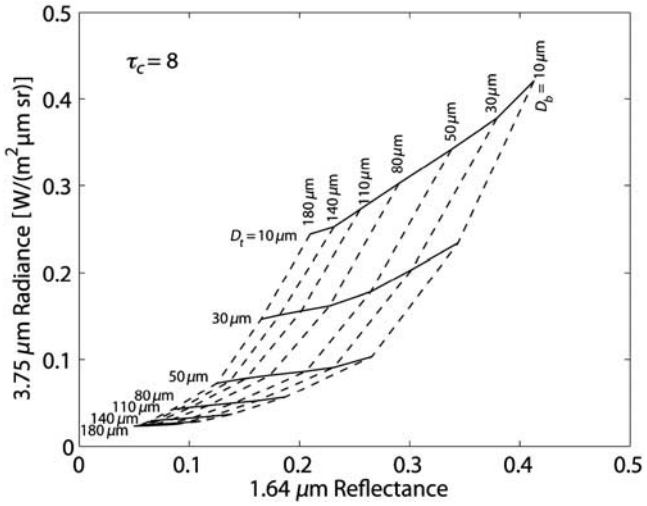


**Figure 3.** Correlation between 1.64 $\mu$m reflectance and 3.75 $\mu$m radiance for selected combinations of $D_t$ and $D_b$ with $\tau_c = 8$.

single-scattering properties. Retrieval errors are obtained as differences between retrieved and input (truth) cloud parameters. Since all reflectance/radiance values are from simulations based on unperturbed input parameters with zero instrument noise, the retrieval errors produced indicate the accuracy of the numerical iteration process. The conditions under which the algorithm is able to perform well are thus identified. We found that for $2 < \tau_c < 15$ and $D_t < 80$ $\mu$m, the retrieval results are reasonably accurate. The root-mean-square (rms) error of retrieved $D_t$, $D_b$ and $\tau_c$ are around 2.4 $\mu$m, 2.8 $\mu$m and 0.004, respectively. These error magnitudes for particle sizes and optical thicknesses are comparable with error estimates for inferred $\tau_c$ and $D_e$ from MODIS cloud retrieval algorithm [*King et al.*, 1997].

[23] For $D_t > 80$ $\mu$m, the accuracy of the retrieval algorithm is limited by the low sensitivity of near-IR reflectance to $D_t$ and $D_b$. Figure 3 displays the correlation of 1.64 $\mu$m reflectance and 3.75 $\mu$m radiance for $\tau_c = 8$, selected combination of $D_t$ and $D_b$, and a prescribed viewing geometry ($\mu = 1$, $\mu_0 = 0.82$, $\Delta\varphi = 180°$). Solid and dashed curves denote reflectance/radiance for constant $D_t$ and $D_b$, respectively. The constant $D_t$ and constant $D_b$ curves are distinctly separated for $D_t < 80$ $\mu$m, indicating a good sensitivity of reflectance/radiance to $D_t$ and $D_b$, and small retrieval errors due to uncertainties in observed reflectance/radiance ($\Delta D_t \sim 2.6$ $\mu$m, $\Delta D_b \sim 3.5$ $\mu$m, see Table 1). However, for $D_t > 80$ $\mu$m, the constant $D_t$ and constant $D_b$ curves are close to each other, implying that a small perturbation of reflectance/radiance can cause an unacceptable error in both retrieved $D_t$ and $D_b$. We estimate that a 5% uncertainty in the 1.64 $\mu$m reflectance can lead to errors of 5 to 20 $\mu$m and 20 $\mu$min the retrieved $D_t$ and $D_b$, respectively.

### 3.2. Retrieval Sensitivity to Uncertainty in Input Parameters and Instrument Noise

[24] The accuracy of the retrieval depends on the accuracy of input parameters $A_g$, $T_c$, $T_g$ and $P_c$, and instrument noise of measured reflectance/radiance. To investigate the error budget due to uncertainties in input parameters along with noises in reflectance/radiance data, we carried out synthetic retrievals with perturbed input parameters and simulated reflectance/radiance. The perturbation of input parameters is based on the following error specifications in MODIS data products: $\Delta T_g = \pm 1$ K, $\Delta P_c = \pm 50$ mb, and $\Delta T_c = \pm 5$ K. For each band, $\Delta A_g = \pm 10\%$, and the perturbation of simulated reflectance/radiance is based on the design-specified signal-to-noise ratio. For each perturbation run, only a single input parameter or reflectance/radiance for a band is perturbed, while all other input parameters and reflectances/radiances are unperturbed. In this manner, we can identify major error sources for each retrieved cloud parameter. On the basis of results for the algorithmic error analysis, synthetic retrievals were carried out for $D_t < 80$ $\mu$m and $2 < \tau_c < 15$. The restriction on $\tau_c$ is due to the fact that retrieval performance deteriorates for either $\tau_c < 2$ or $\tau_c > 15$. The retrieval is most effective for semitransparent cirrus clouds.

[25] Table 1 summarizes the absolute and percentage RMS errors of retrieved $D_t$, $D_b$, and $\tau_c$ subject to various single-parameter perturbations. Most of the RMS errors are comparable with error budget estimates of $\tau_c$ and $D_e$ for the cloud optical property retrieval program using the solar channels of the Visible Infrared Imaging Radiometric Suites (VIIRS), which is to be onboard the next generation National Polar-Orbiting Environmental Satellite System (NPOESS) [*Ou et al.*, 2003]. Retrievals of $\tau_c$ are fairly accurate with the maximum RMS percentage errors around 3% associated with $\Delta A_g(0.645\ \mu\text{m}) = \pm 10\%$, indicating the accuracy of the visible band surface albedo drives the retrieval performance of $\tau_c$. Retrievals of $D_t$ and $D_b$ are also reasonably accurate, with the largest errors around 10 and 14 $\mu$m associated with $\Delta T_c = \pm 5$ K, respectively. It is possible that with future

**Table 1.** Root-Mean-Square Error of Synthetic Retrievals Subject to Perturbation to Input Parameters and Instrument Noise[a]

| Perturbed | rms ($\Delta\tau_c$) | rms [($\Delta\tau_c/\tau_c$) × 100%] | rms ($\Delta D_t$) | rms [($\Delta D_t/D_t$) × 100%] | rms ($\Delta D_b$) | rms [($\Delta D_b/D_b$) × 100%] |
|---|---|---|---|---|---|---|
| $P_c$ (50 mb) | 0.016 | 0.16 | 2.55 | 4.5 | 3.05 | 15.3 |
| $T_s$ (1 K) | 0.007 | 0.12 | 3.58 | 8.6 | 4.87 | 21.1 |
| $T_c$ (5 K) | 0.061 | 0.66 | 10.39 | 18.4 | 14.03 | 23.8 |
| $A_{g,1}$ (10%) | 0.138 | 3.20 | 4.13 | 9.1 | 5.06 | 19.4 |
| $A_{g,2}$ (10%) | 0.030 | 0.80 | 5.91 | 15.7 | 11.38 | 34.3 |
| $A_{g,3}$ (10%) | 0.018 | 0.49 | 3.87 | 10.0 | 7.38 | 24.3 |
| $A_{g,4}$ (10%) | 0.004 | 0.1 | 2.64 | 5.4 | 3.31 | 14.1 |
| $R_1$ (SNR = 128) | 0.144 | 1.6 | 2.75 | 5.2 | 3.53 | 16.3 |
| $R_2$ (SNR = 275) | 0.008 | 0.10 | 2.58 | 4.7 | 3.20 | 15.6 |
| $R_3$ (SNR = 110) | 0.016 | 0.18 | 2.65 | 5.0 | 3.62 | 16.3 |
| $R_4$ (SNR = 200) | 0.009 | 0.09 | 2.65 | 4.98 | 3.33 | 15.7 |

[a]The definition of the notations are as follows: $P_c$, cloud top pressure; $T_s$, surface temperature;, $T_c$, cloud temperature; $A_g$, surface albedo; $R$, measured reflectance.

satellite sensors, such as VIIRS/NPOESS, the specified uncertainty for $T_c$ could be further reduced. MODIS specified 5 K uncertainty in $T_c$ is caused by the deficiency in the $CO_2$ slicing method that MODIS cloud top parameter algorithms adopted [*Menzel et al.*, 2006]. MODIS $T_c$ are often positively biased near cirrus cloud edge because of the effect of the 5 × 5 pixel aggregation, which might include clear pixels mistyped as cloudy pixels, increasing the averaged cloudy radiance, and hence overestimating the cloud top pressure and temperature [*Wong et al.*, 2007]. According to the new design specification of NPOESS/VIIRS, the uncertainty threshold requirement for $T_c$ is 3 K, and has been met on the pixel level by the VIIRS cloud top temperature retrieval program (E. K. Wong and S. C. Ou, NPOESS/VIIRS cloud top temperature–Algorithm performance case study, paper presented at 4th Symposium on Future National Operational Environmental Satellites, American Meteorological Society, New Orleans, Louisiana, 2008). Given the smaller uncertainty in $T_c$ based on VIIRS retrieval, errors in retrieved $D_t$ and $D_b$ can be reduced by half.

## 4. Retrieval Results and Validation

[26] This section presents results of the application of the retrieval algorithm to three MODIS cirrus cases, and of the assessment of retrievals using data sets from MMCR and CPR/CloudSat. The first scene over south central United States was observed by MODIS/Terra, and the quality of its retrieval results were evaluated by comparing with MODIS cloud products and cloud properties derived from MMCR data. The second and third cirrus scenes over north central China and northeast Asia, respectively, were observed by the A Train's MODIS/Aqua and CPR/CloudSat, and retrieval results are compared with MODIS and CPR data products.

[27] We have attempted to compare the retrieved $D_t$, $D_b$ and $\tau_c$ and those parameters from CALIOP/CALIPSO cloud products for the last two cases. However, because of the nonabsorbing nature of the CALIOP operating laser wavelengths, there is no data product for cloud effective particle size, and we cannot use CALIOP data to verify our retrieved $D_t$ and $D_b$. On the other hand, CALIOP data products do include extinction coefficient ($\beta_e$) profiles, which could be vertically integrated to produce $\tau_c$, and could be used to verify retrieved $\tau_c$. But for opaque clouds, because of the laser's limited penetration, CALIOP $\tau_c$ tend to be much smaller than retrieved $\tau_c$, and the resulting time series of $\tau_c$ tend to be insensitive to the horizontal inhomogeneiry of clouds. Therefore, it is not adequate to use CALIOP $\tau_c$ to assess the retrieved $\tau_c$.

### 4.1. ARM-SGP Site (6 March 2001 at 1736 UTC)

[28] On 6 March 2001 at 1736 UTC, MODIS/Terra overpassed the ARM-SGP Central Facility site (CF) at Lamont (36.62°N, 97.5°W) with excellent viewing zenith angle ($\theta$ = 1.3°). The MODIS true color composite image (Figure 4a) shows a large area of stratiform cirrus clouds over the south central United States. The operational MMCR at CF also observed a continuous layer of cirrus cloud between 6 and 11 km during the period from 0600 to 2200 UTC. For the purpose of assessing retrieval results by comparison with MODIS and MMCR cloud products, we selected a rectangular domain (51 × 51 pixels, denoted by the red rectangular box in Figure 4a) around CF, which is roughly located in the center of the rectangular box in Figure 4a. Cloud mask result indicates that pixels within the box are cloudy, and the cloud phase results as determined by the cloud phase mask program and extracted from the MOD06 cloud product [*Menzel et al.*, 2006] show that these cloudy pixels are cirrus clouds. Cloud–top temperatures for cirrus pixels are lower than 240 K.

[29] The retrieval algorithm is applied to each cirrus cloud pixel within the domain, and mappings of retrieved $\tau_c$, $D_t$ and $D_b$ are shown in Figures 4b–4d, respectively. The $\tau_c$ values (∼6) over the northwest quadrant is relatively large, while small $\tau_c$ values (<3) over the southeast quadrant indicate optically thin cirrus clouds. Except for the northwest quadrant, retrieved $D_t$ values (∼50 $\mu$m) are generally smaller than $D_b$ (>150 $\mu$m), consistent with in situ observed stratified pattern as described in section 1. The vertically mean $\overline{D}_e$ for each pixel from the retrieval is calculated by the average of $D_t$ and $D_b$. Comparison with MODIS cloud products reveals that retrieved (Figure 4b) and MODIS $\tau_c$ maps are almost identical, but retrieved $\overline{D}_e$ [= $(D_t + D_b)/2$] are systematically larger than MODIS $\overline{D}_e$ (= $2r_e$), which were extracted from the MODIS cloud effective particle size products retrieved using 0.645 $\mu$m (band 1) and 2.13 $\mu$m (band 7) reflectances.

[30] Scatterplots in Figures 4e and 4f show the correlation between retrieved and MODIS $\tau_c$ and $\overline{D}_e$ for the selected domain, respectively. Figure 4e shows retrieved and MODIS $\tau_c$'s are highly correlated, with a correlation coefficient of 0.983, and this good correlation demonstrates that the retrieved $\tau_c$ is highly accurate. The RMS difference is 0.219, which is about 5% of the mean $\tau_c$ (∼4), and is comparable to the objective requirement for NPOESS-VIIRS algorithm [*Ou et al.*, 2003]. Figure 4f shows that the retrieved mean $\overline{D}_e$ also correlates well with MODIS $\overline{D}_e$ with a correlation coefficient of 0.65. Differences for the retrieved and MODIS $\overline{D}_e$ are due primarily to the differences in the assumed vertical $D_e$ profiles. In the present radiative transfer program to generate the look-up library, the vertical linear profile of $D_e$ has been included in the calculations, whereas in the MODIS forward radiative transfer modeling, cloud effective particle size is assumed to be vertically constant. Thus, retrieved $\overline{D}_e$ are mostly larger than MODIS $\overline{D}_e$, because, with the assumption that the vertical distribution of $D_e$ increases from the cloud top toward the cloud base, MODIS $\overline{D}_e$ tends to be biased toward the smaller cloud top $D_e$ as indicated by Figure 1, while the retrieved $\overline{D}_e$ tends to be biased toward the larger midcloud $D_e$. Since both the present and MODIS 005 Collection algorithms have employed the same ice crystal size and habit distribution models, the difference between the mean effective particle sizes inferred from the present and MODIS retrieval programs should not be due to difference in the assumption of ice crystal habits.

[31] Around the time of the Terra overpass, the MMCR at CF also observed a single layer of cirrus clouds between 6 and 10 km. Figure 5a shows the MMCR time series of vertically resolved $D_e$ [*Mace et al.*, 2002]. Over a 10 min period (5 min before and after the MODIS overpass), MMCR observed 16 $D_e$ profiles. The MMCR $D_e$ vary between 50 and 150 $\mu$m, with a few spots larger than 150 $\mu$m.

[32] To assess the validity of retrieved $D_t$ and $D_b$, we processed MMCR $D_e$ and IWC profiles, and applied a collocation scheme to the retrieved cloud parameters. For each of the

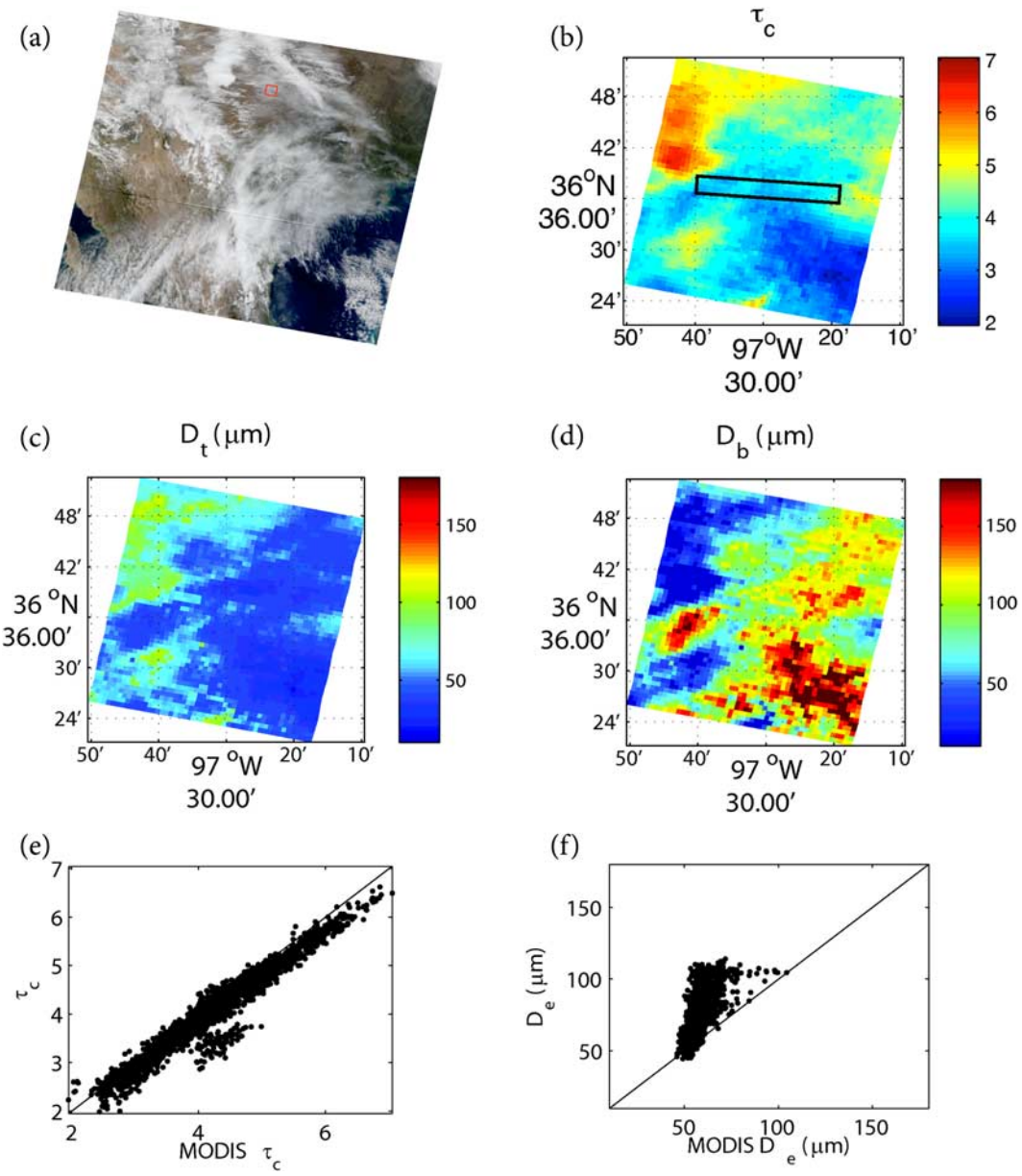


**Figure 4.** (a) MODIS true color composite images for 6 March 2001 at 1736 UTC, (b) retrieved $\tau_c$, (c) retrieved $D_t$ for selected domain, (d) retrieved $D_b$ for selected domain, (e) scatterplot for retrieved $\tau_c$ versus MODIS $\tau_c$ for selected domain, and (f) scatterplot for retrieved $D_e$ versus MODIS $D_e$ for selected domain. The black rectangle in Figure 4b denotes a 2 × 16.8 km strip of cloud that is supposed to have drifted over the MMCR site during the 10 min period and has been scanned by the radar beam.

16 MMCR profiles, we first obtained the vertical profile of extinction coefficient $\beta_e(z)$ as [*Fu and Liou*, 1993]

$$\beta_e(z) \approx \mathrm{IWC}(z)[a + b/D_e(z)], \tag{10}$$

where $a = -6.656 \times 10^{-3}$, $b = 3.686$, $\beta_e(z)$ is in the unit of $\mathrm{m}^{-1}$, IWC in g $\mathrm{m}^{-3}$ and $D_e$ in $\mu$m. Then $\tau(z)$ is calculated by the vertical integration of $\beta_e$ $(z)$ from cloud top to the level $z$

$$\tau(z) = \int_z^{z_t} \beta_e(z)dz. \tag{11}$$

Finally, the MMCR $D_e(z)$ is converted to $D_e(\tau)$ using $\tau(z)$. A linear fitting procedure is applied to each $D_e(\tau)$ profile to generate $D_t$ and $D_b$. The MMCR time series of $D_t$ and $D_b$ are plotted as lines with triangle symbols in Figures 5b and 5c, respectively.

[33] We then applied a space-to-time collocation scheme to match the geographical locations of retrieved $D_t$ and $D_b$ with the observation time of MMCR $D_e$ profiles. Since the MODIS data represent nearly instantaneous observation on the order of only a few seconds, while the MMCR data provide a time series of observations from a single location, we can establish the space-to-time correlation between the two data sets by using the wind speed and direction data at the

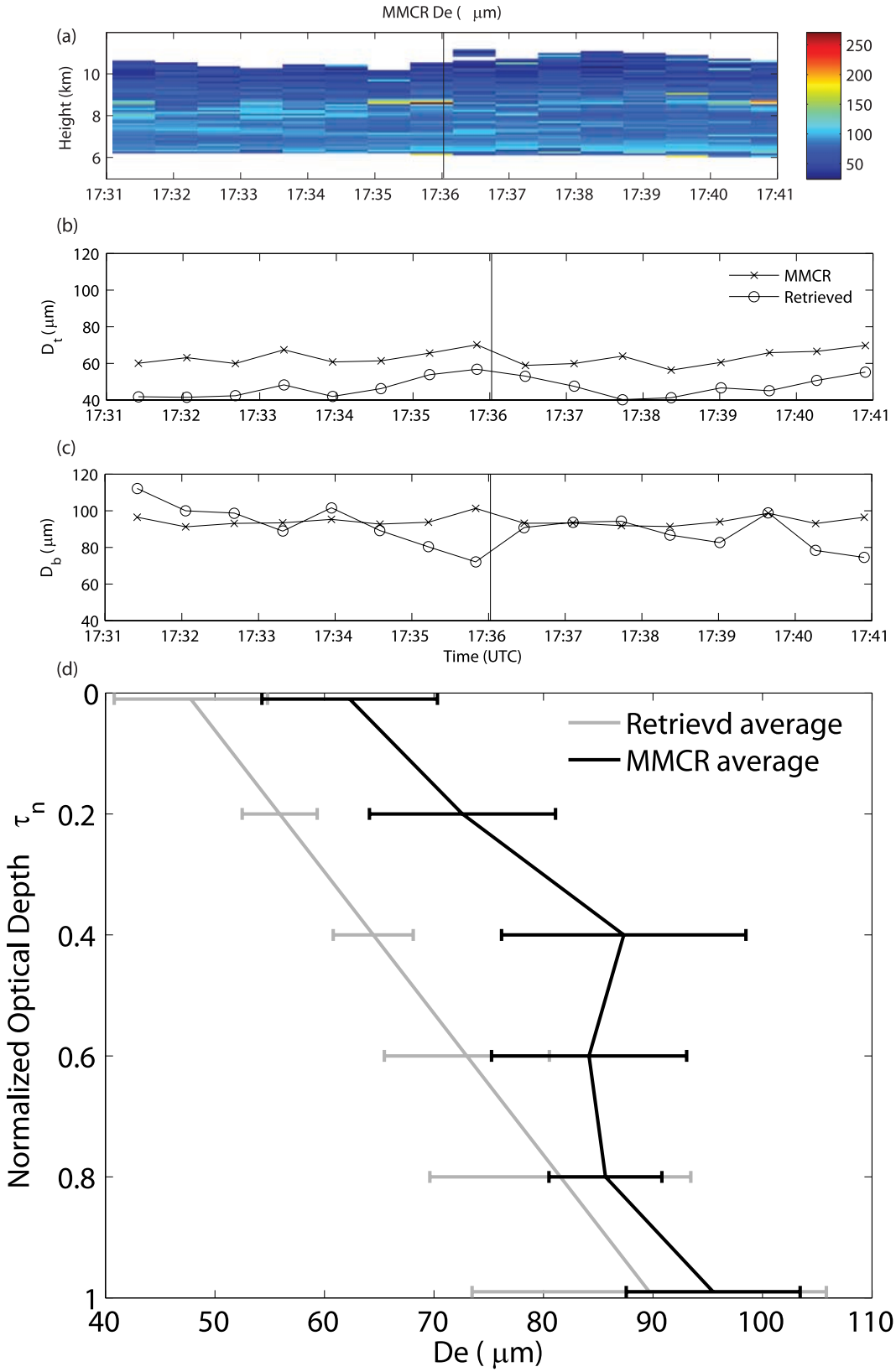


**Figure 5.** (a) Time series of vertically resolved $D_e$ derived from MMCR in the 10 min period centered around the satellite overpass at 1736 UTC on 6 March 2001, which is denoted by the vertical line; (b) collocated time series of retrieved and MMCR $D_t(t)$; (c) same as Figure 5b except for $D_b$; and (d) strip-averaged retrieved (gray curve) and MMCR (black curve) $D_e$ profiles as functions of $\tau_n$. Horizontal bars denote standard deviations.

cirrus cloud level from atmosphere soundings [*Ou et al.*, 1995]. As observed by collocated daytime soundings, which were launched at CF (collocated with the MMCR site) and at 1130 and 2029 UTC, the wind speed and direction at the cirrus cloud level based on interpolation to the MODIS overpass time are estimated to be around 28 m $s^{-1}$ and 276° clockwise from north, respectively. Within the selected domain, we further identified a 2 × 16.8 km strip of cloud (denoted by the black rectangle in Figure 4b) that is supposed to have drifted over the MMCR site during the 10 min period, and has been scanned by the radar beam. The length of the strip is the distance traveled by the cloud within the 10 min period (600s × 28 m $s^{-1}$ = 16,800 m). Then we match the geographical location of each pixel within the strip with the time of one of the 16 MMCR profiles. Because there are altogether 37 pixels within the strip, each MMCR profile may correspond to two or three pixels. Then mean values of retrieved $D_t$ and $D_b$ for collocated pixels associated with each MMCR profile are calculated. The converted and MMCR time series of retrieved $D_t$ and $D_b$ are plotted as curves with circles and crosses in Figures 5b and 5c, respectively.

[34] Figure 5b shows that retrieved and MMCR $D_t$ vary between 40 and 55 $\mu$m, and between 60 and 70 $\mu$m, respectively, and that both time series display similar trends. The MMCR $D_t$ is systematically 10–30 $\mu$m larger than corresponding retrieved values. This difference near cloud top could be explained by the fact that MMCR are mainly sensitive to large particles and missing smaller particles [*Comstock et al.*, 2002]. Since cloud top is generally composed of smaller particles, MMCR derived $D_t$ may be positively biased. Figure 5c displays that retrieved and MMCR $D_b$ vary between 70 and 100 $\mu$m and between 90 and 100 $\mu$m, respectively, and that retrieved $D_b$ displays more variability than MMCR. However, the two $D_b$ series generally agree with each other better than the two $D_t$ series, with differences anywhere between 0 and 30 $\mu$m. This better agreement near cloud base could be due to the fact that MMCR $D_b$ might be less biased than $D_t$, given that particle sizes at cloud base is larger than at cloud top. Similar magnitude and sign of differences between AIRS retrieved and MMCR derived ice crystal sizes were reported by *Yue et al.* [2007].

[35] Figure 5d shows the averaged $D_e$ profiles derived from MMCR observations (black lines) and retrievals (gray lines) as functions of normalized cloud optical depth, $\tau_n$, where $\tau_n$ is defined as

$$\tau_n = \tau/\tau_c. \tag{12}$$

Horizontal bars at the six selected $\tau_n$ levels represent the standard deviations of $D_e$. Both the averaged profiles show that $D_e$ generally increases from the cloud top toward the cloud base, consistent with the general behavior of midlatitude cirrus clouds. The slope of retrieved profile is about 45 $\mu$m per unit $\tau_n$, while the slope of the MMCR profile is around 53 $\mu$m per unit $\tau_n$. Figure 5d demonstrates a qualitative agreement in the vertical trend of retrieved and MMCR $D_e$ profiles. The standard deviations vary between 10 and 20 $\mu$m for the MMCR profiles, and they increase from upper cloud (~10 $\mu$m) to lower cloud (~30 $\mu$m).

[36] In addition to the remote sensing characteristics of MMCR, differences between retrieved and MMCR retrievals can also be attributed to other factors involving spatial coverage and microphysical processes. The spatial coverage for MODIS is considerably different from MMCR. MODIS has a nominal spatial resolution of 1 km near nadir. MMCR deployed at ARM-SGP site has a beam diameter of 3 m at ground level and beam width of 0.19°. The beam diameter increases to 22 m at 6 km and 36 m at 10 km. The MMCR beam diameters are much smaller than MODIS pixel sizes. Difference in retrieved and MMCR derived cloud particle size parameters can result from different observation scales. Moreover, in our collocation scheme, we assume that cirrus clouds drifted over the MMCR site with nearly constant bulk microphysics properties over the 10 min period. However, the temporal scale of cloud microphysical processes is on the order of seconds, so the evolution of clouds can be another source of differences in retrieved and MMCR cloud parameters.

### 4.2. North Central China (17 October 2006 at 0624 UTC)

[37] MODIS/Aqua flew over north central China on 17 October 2006, at 0624 UTC, followed by CloudSat. The MODIS true color composite image (Figure 6a) contains an area of widespread stratiform cirrus clouds over the Inner Mongolia region. The black solid line denotes the CloudSat orbital track. For comparison with MODIS cloud products from Collection 005 algorithms and for assessment of retrieval results using CPR data, we selected a strip of cloudy area (26 × 301 pixels) centered along the CloudSat track, as indicated by the red narrow rectangular box. The MODIS cloud mask result indicates that most pixels within the box are cloudy, and cloud phase product shows that the majority of cloudy pixels in the box are cirrus clouds. Cloud–top temperatures for cirrus pixels are lower than 240 K.

[38] Figures 6b–6d show retrieved $\tau_c$, $D_t$ and $D_b$ for the selected box, respectively. The $\tau_c$ values are small (<5) over the northern part of the box, indicating the presence of thin cirrus clouds, and $\tau_c$ values are large (~30) over the southern part of the box, showing the occurrence of opaque cirrus clouds. The size parameters $D_t$ and $D_b$ vary between 0 and 120 $\mu$m and between 0 and 180 $\mu$m, respectively, and $D_t$ are generally smaller than $D_b$, except for the central part of the box, where $D_t$ are around 120 $\mu$m, and are larger than $D_b$. Figures 6e and 6f show the correlation between retrieved and MODIS $\tau_c$ and $\overline{D}_e$, respectively, for cloud-mask-identified cirrus cloud pixels, for which both vertical sizing retrievals and MODIS products are available. The retrieved and MODIS mean sizes $\overline{D}_e$ have been defined in section 4.1. The vertical sizing retrieval results are highly correlated with the MODIS cloud products, with correlation coefficients for $\tau_c$ and $\overline{D}_e$ being 0.96 and 0.803, and the RMS differences being 1.03 and 29.4 $\mu$m, respectively. Retrieved $\tau_c$ values agree well with MODIS for $\tau_c < 20$, but retrieved $\overline{D}_e$ are generally larger than MODIS $\overline{D}_e$. The possible explanation for such a behavior has been given in section 4.1. It is noted that the geographical distribution of retrieved $\tau_c$ (Figure 6b) and $\overline{D}_e$ are both similar to those of MODIS $\tau_c$ and $\overline{D}_e$.

[39] To compare vertical sizing retrieval results with collocated CPR data products within the selected cloudy box, we further identified two parts of the CloudSat track, where the CloudSat observed cirrus cloud coverage is continuous. The lower and upper sections are indexed as Segments 1 and 2, respectively, as denoted by the two yellow lines in Figure 6b.

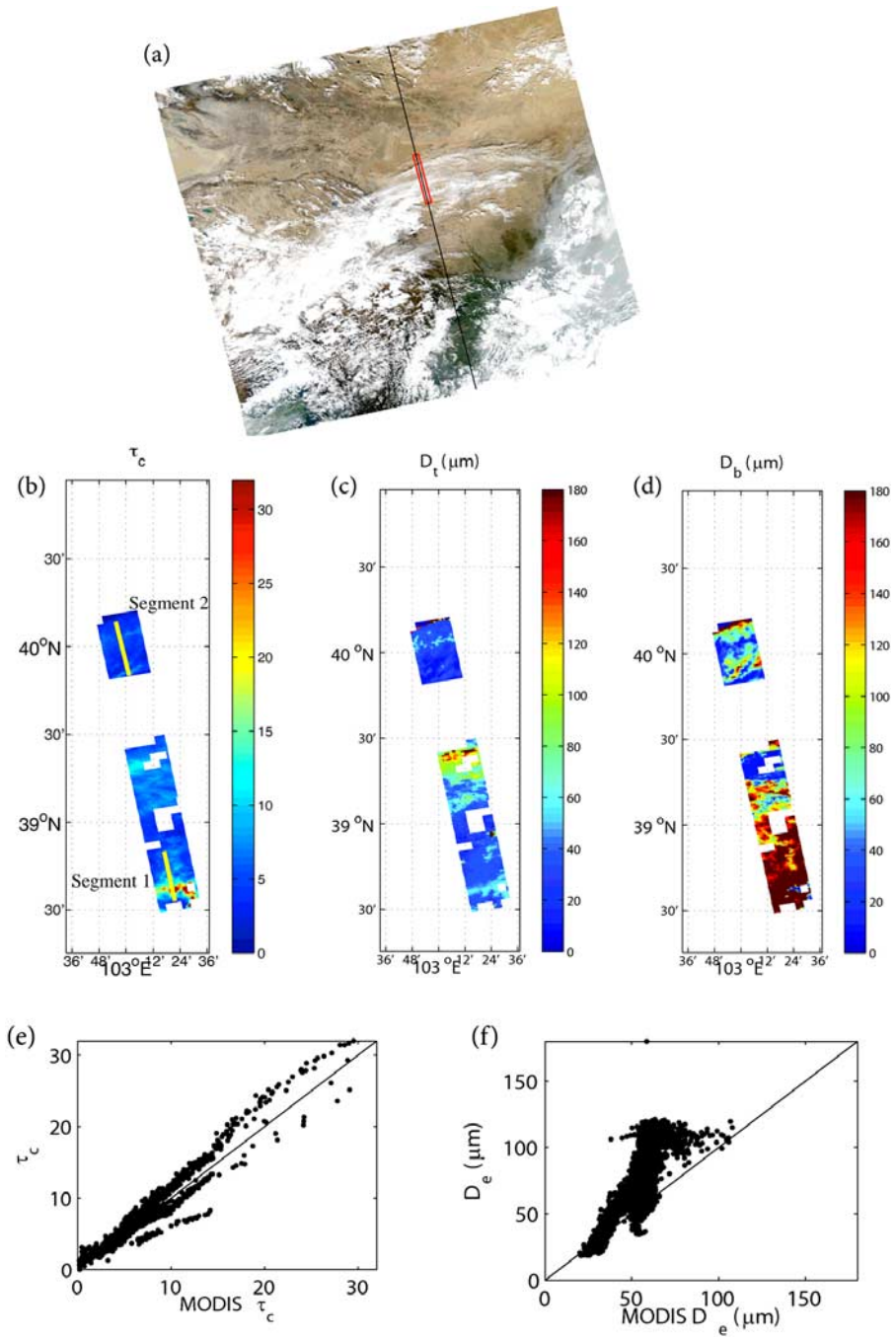


**Figure 6.** (a) MODIS true color composite images for 17 October 2006 at 0624 UTC, over north central China; (b–f) same as Figures 4b–4f except for this case.

Segments 1 and 2 correspond to CloudSat 5 and 3 s overpasses, respectively. The vertically resolved cloud effective radius and cloud liquid/ice water content derived from CPR backscatter data have been archived in the 2B-CWC-RO data product, where "CWC-RO" means Radar-Only Combined Water Content.

[40] The bulk microphysical properties of clouds were assumed to remain largely constant within the 1 min gap between Aqua and CloudSat/CALIPSO overpasses. We compared the retrieved cloud size parameters with the CloudSat data products. The CPR time series of vertically resolved $D_e$ for Segments 1 and 2 are presented in Figures 7a and 7b, respectively. The CPR time series of $D_t$ and $D_b$ were derived in the same manner as for MMCR, and were collocated with retrieved $D_t$ and $D_b$. Because each CPR footprint roughly covers 15 MODIS pixels [3 (cross track) × 5 (along track)], we computed the average of retrieved $D_t$ and $D_b$ for the 15 MODIS pixels, and compared them with the collocated CPR $D_t$ and $D_b$.

[41] Results of comparison of $D_t$ and $D_b$ for Segment 1 are shown in Figures 7c and 7e, respectively. Retrieved $D_t$ and $D_b$ are generally smaller than CPR $D_t$ and $D_b$, because, like MMCR, CPR observations tend to miss the smaller particles in cirrus clouds. Moreover, differences between retrieved and

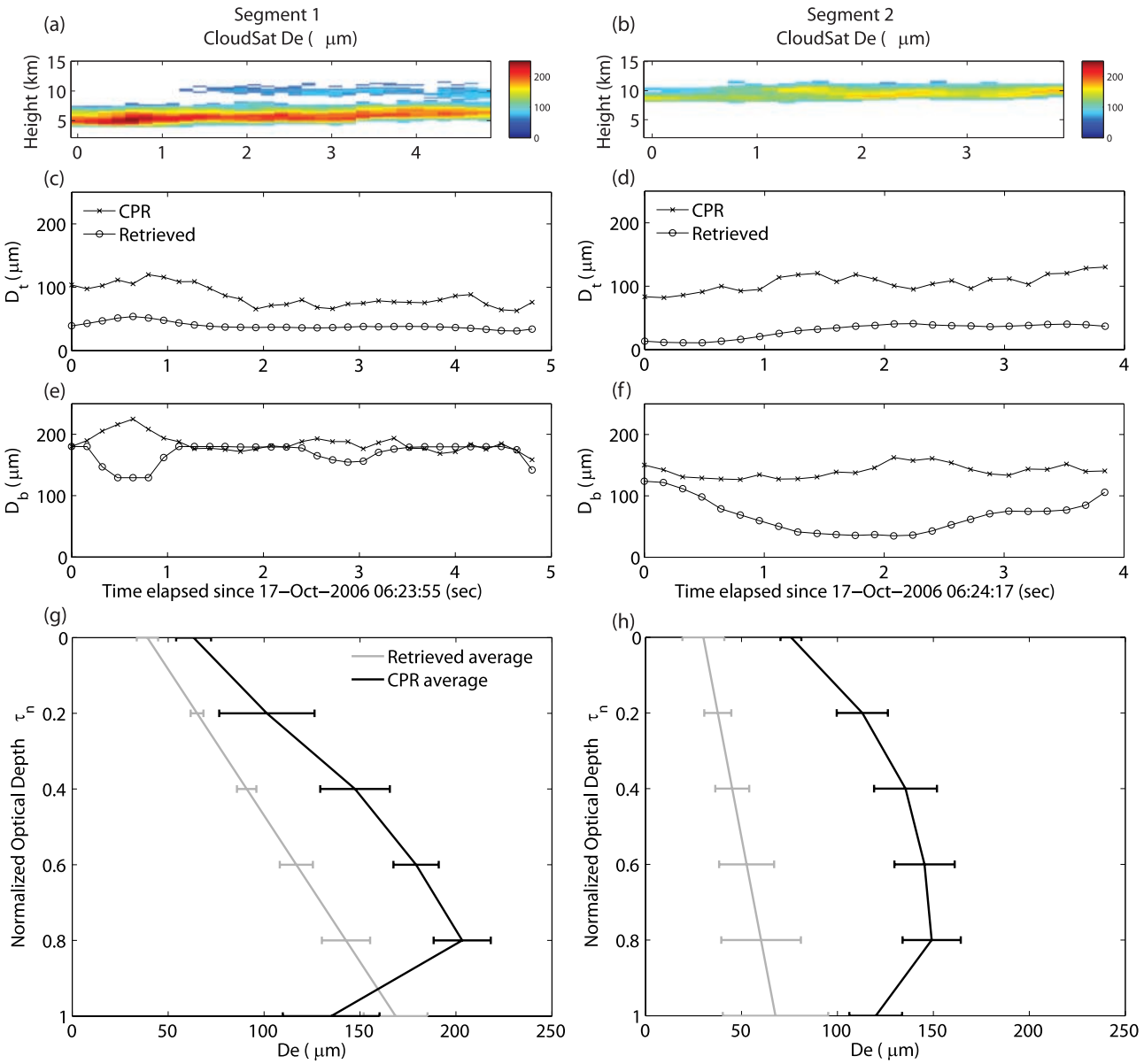


**Figure 7.** (a and b) Time series of vertically resolved $D_e$ derived from CPR observations for Segments 1 and 2, respectively; (c and d) collocated time series of retrieved and CPR $D_t(t)$ for Segments 1 and 2, respectively; (e and f) are same as Figures 7c and 7d, respectively, except for $D_b$; and (g and h) segment-averaged retrieved (gray curve) and CPR (black curve) $D_e$ profiles as functions of $\tau_n$ for Segments 1 and 2, respectively, where horizontal bars denote standard deviations.

CPR $D_b$ (Figure 7e) are smaller than those for $D_t$. This is because CPR $D_t$ are smaller than CPR $D_b$, and therefore, we expect more small particles near cloud top were missed by CPR observations than at cloud base, and the agreement for $D_b$ is better than for $D_t$. Results of comparison of $D_t$ and $D_b$ for Segment 2 are shown in Figures 7d and 7f, respectively. Like the comparison for Segment 1, retrieved $D_t$ and $D_b$ are generally smaller than those from CPR. Differences for $D_t$ and $D_b$ vary between 50 and 80 $\mu$m and between 30 and 100 $\mu$m, respectively. The larger ranges of differences for $D_t$ and $D_b$ in Figures 7d and 7f than in Figures 7c and 7e could be due to the lower accuracy in the retrieved effective particle sizes at smaller optical depths for Segment 2 as shown in Figure 6b [*Ou et al.*, 2003].

[42] Comparisons of the retrieved average (gray curves) and CPR (dark curves) $D_e$ profiles for Segments 1 and 2 are shown in Figures 7g and 7h, respectively, where horizontal bars represent standard deviations of $D_e$. For both segments, both retrieved and CPR $D_e$ generally increase from cloud top toward cloud base, and the gradient of increase for both retrieved and CPR $D_e$ in Segment 1 are larger than in Segment 2. The CPR $D_e$ in both segments recurves toward smaller values near cloud base, consistent with typical in situ observation. This feature cannot be reproduced by the present retrieval scheme because of the linear constraint of the vertical size profile. Nevertheless, the slope of increase for retrieved $D_e$ roughly agrees with the CPR $D_e$. Differences between retrieved and CPR $D_e$ in Segment 2 is generally

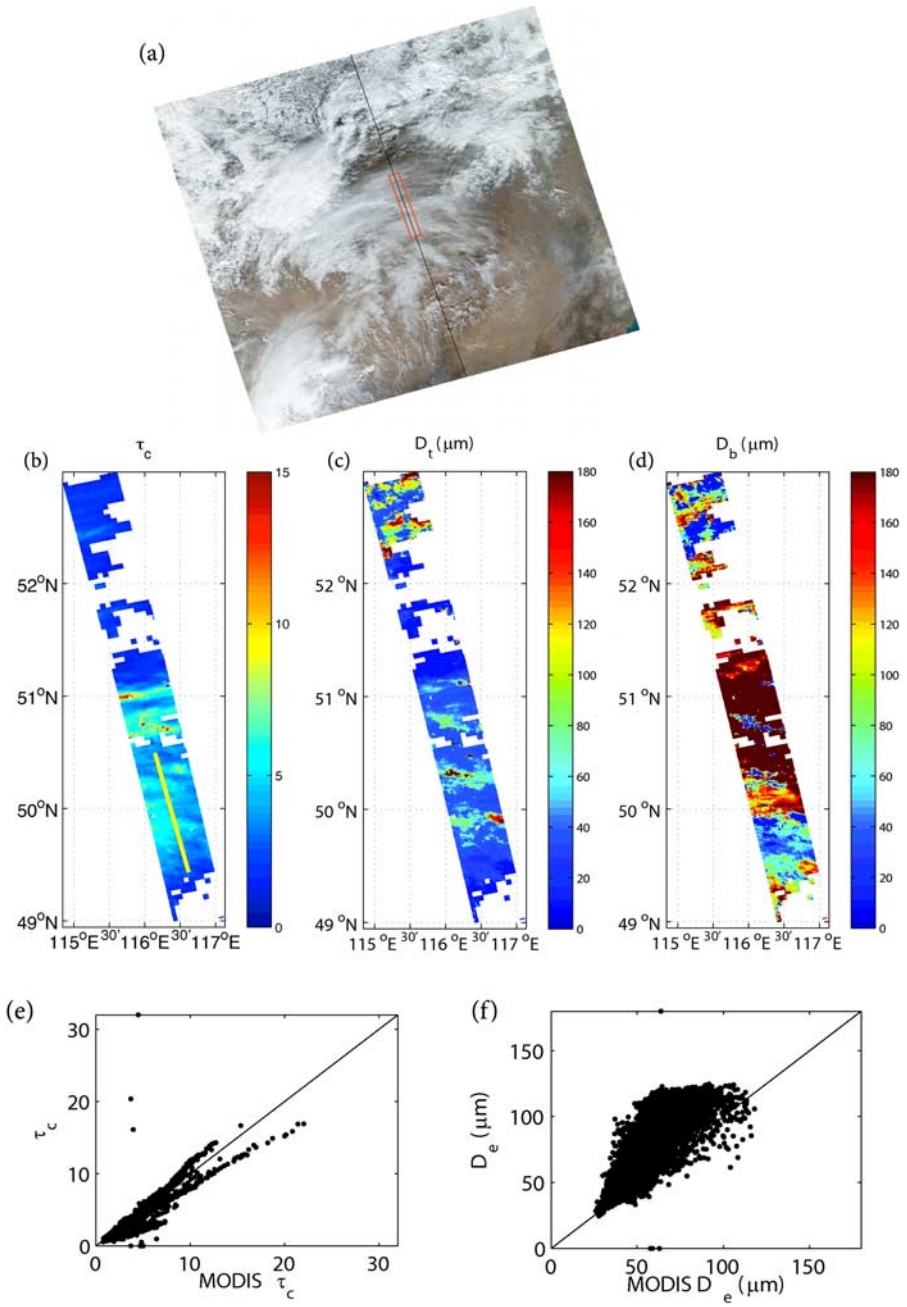


**Figure 8.** (a) MODIS true color composite images for 23 October 2007 at 0515 UTC, over northeast Asia; (b–f) same as Figures 4b–4f except for this case.

larger than in Segment 1. As also shown by Figures 7c–7f, the agreement for Segment 1 is better than for Segment 2. These behaviors can be explained by the fact that a large portion of CPR $D_t$ is generally less than 80 $\mu$m, while most CPR $D_b$ are larger than 80 $\mu$m. As indicated by Figure 3, the retrieval performs effectively for $D_t < 80$ $\mu$m, and therefore, we expect the vertical sizing retrievals to agree with CPR product better for Segment 1 than for Segment 2.

### 4.3. Northeast Asia (23 October 2007 at 0515 UTC)

[43] MODIS/Aqua flew over northeast Asia around 0515 UTC on 23 October 2007, followed by CloudSat. The MODIS true color composite image (Figure 8a) displays a large area of stratiform cirrus clouds over Eastern Siberia. The black line denotes the CloudSat track. As in the case of 17 October 2006, for the purpose of assessment of retrieval performance using CPR observations, a narrow area (51 × 451 pixels) centered along the CloudSat track has been selected, as indicated by the red rectangular box. Cloud mask result indicates that most pixels within the box are cloudy, and cloud phase product shows that the majority of cloudy pixels are cirrus clouds. Cloud top temperatures for cirrus pixels are lower than 240 K.

[44] Figures 8b–8d show retrieved $\tau_c$, $D_t$ and $D_b$ products for the selected box, respectively. For the whole box, $\tau_c < 5$, and both $D_t$ and $D_b$ vary between 0 and 180 $\mu$m, with most $D_t < D_b$, except several small areas around north and south parts of the box. Scatterplots in Figures 8e and 8f

show the correlation between retrieved and MODIS $\tau_c$ and $\overline{D}_e$, respectively, for pixels for which both the vertical sizing retrieval and MODIS cloud product from Collection 005 algorithms are available. Retrieved $\tau_c$ and $D_e$ are highly correlated with MODIS cloud products, with correlation coefficients being 0.947 and 0.743, and RMS differences being 0.662 and 29.6 $\mu$m, respectively. Similar to the 6 March 2001 and 17 October 2006 cases, the retrieved $\tau_c$ appear to agree qualitatively with MODIS $\tau_c$, and the correlation between retrieved and MODIS $\overline{D}_e$ is also significant with retrieved $\overline{D}_e$ generally larger than MODIS values. The possible explanation for such behavior has been given in section 4.1.

[45] To compare retrieval results with collocated CPR data products within the selected box, we further identified a section of the CloudSat track, in which the cirrus cloud coverage is continuous. This section corresponds to a 10 s CloudSat overpass from 0518:30 to 0518:40 UTC, and is denoted by the yellow line segment in Figure 8b. The procedure for the processing of the CPR data is the same as in the 17 October 2006 case. The CPR time series of vertically resolved $D_e$ are presented in Figure 9a. Particles with sizes smaller than 100 $\mu$m are present at cloud top, while near cloud base, particles are much larger (>200 $\mu$m). Time series of retrieved average and CPR $D_t$ and $D_b$ are shown in Figures 9b and 9c, respectively. The time series of CPR $D_t$ are relatively constant without too much oscillations, and are consistent with cloud top $D_e$ values shown in Figure 9a. The increase in retrieved $D_t$ between $t = 6-8$ s actually matches the CPR $D_t$ values. Both retrieved $D_t$ and $D_b$ are generally smaller than collocated CPR data, because of CPR's inability to detect smaller ice crystals. Differences in $D_b$ are smaller than those in $D_t$, because of the presence of more large particles at cloud base than at cloud top (see Figure 9a). We also examined the retrieved average vertical profiles of $D_e$ with CPR as a function of normalized cloud optical depth $\tau_n$. Figure 9d shows the retrieved average (gray line) and CPR (dark line) $D_e$ profiles, where horizontal bars represent standard deviations of $D_e$. For this region, effective particle sizes generally increase from cloud top to cloud base.

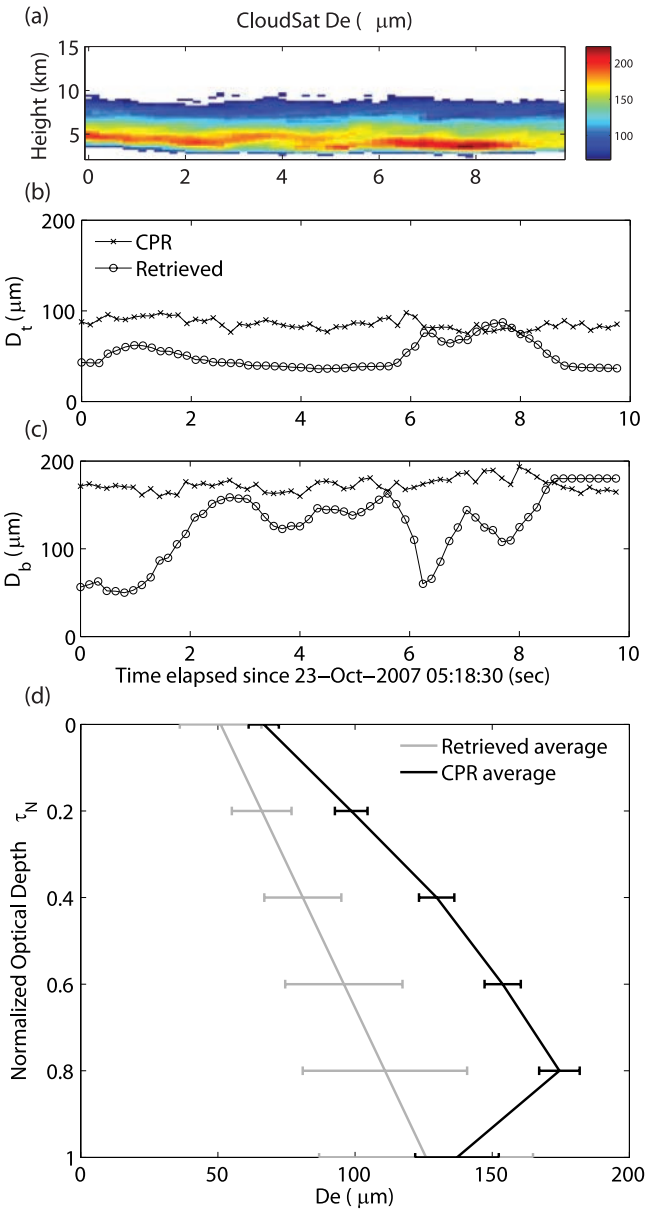


**Figure 9.** (a) Time series of vertically resolved $D_e$ derived from CPR observations; (b) collocated time series of retrieved and CPR $D_t(t)$; (c) same as Figure 9b, except for $D_b$; (d) section-averaged retrieved (gray curve) and CPR (black curve) $D_e$ profiles as functions of $\tau_n$, where horizontal bars denote standard deviations.

## 5. Summary

[46] Detailed analyses of in situ balloon-borne ice crystal observations reveal that cirrus clouds are often vertically stratified, with small quasi-spherical or plate-like particles at the cloud top, hexagonally shaped and bullet rosettes crystals in the midcloud layers, and large and irregularly shaped single or aggregated particles near the cloud base. Radiative transfer simulations indicate that heating/cooling within cirrus clouds is driven by the vertical distribution of cloud particle sizes and shapes. Clearly, in order to accurately determine cloud radiative forcing and heating/cooling rate for the study of climate change, it is necessary to have comprehensive and reliable knowledge of the vertical profile of cloud particle sizes. Current MODIS cirrus cloud retrieval algorithm assumes a vertically homogeneous cloud model to retrieve the total cloud optical thickness and vertically averaged effective particle size. With the availability of multiple near-IR band radiance data from MODIS, it appears that a retrieval scheme for inferring the vertical ice crystal sizes over large areas could be developed utilizing the information content in near-IR bands on the basis of the difference in cloud absorption for each band.

[47] In this paper, we present a cirrus cloud vertical sizing algorithm to infer the cloud top and cloud base mean effective particle sizes from a combination of MODIS visible and near-IR band reflectance/radiance, where the vertical profile of ice crystal size is linearly constrained as a function of optical depth. This approach uses a numerical iterative search method based on a look-up library of precomputed reflectances/radiances from an adding-doubling radiative transfer program, subject to corrections for Rayleigh scattering at the 0.645 $\mu$m

band, above-cloud water vapor absorption, and 3.75 $\mu$m thermal emission.

[48] The performance and limitation of the retrieval method were investigated by synthetic retrievals. Retrieval results are reasonably accurate for $2 < \tau_c < 15$ and $D_t < 80$ $\mu$m. For $D_t > 80$ $\mu$m, the accuracy decreases because of the decrease in sensitivity of the near-IR reflectance to $D_t$ and $D_b$. An error budget analysis of the retrieval algorithm subject to the perturbation of input cloud temperature, cloud top pressure, surface temperature and surface albedos and to instrument noise was also carried out by synthetic retrievals. Retrievals of $\tau_c$ are relatively accurate with the largest RMS percentage error around 3% when the 0.645 $\mu$m band surface albedo is perturbed by ±10%. The RMS error of retrieved $\tau_c$ value is roughly 0.16. The retrieval accuracy of $D_t$ and $D_b$ is subject to the 3.75 $\mu$m band radiance noise and the retrieved $D_t$ and $D_b$ value has an estimated RMS error of about 20 and 28 $\mu$m, respectively.

[49] The retrieval algorithm was applied to three MODIS cirrus scenes over the ARM-SGP site, north central China, and northeast Asia. The accuracy of retrieved cloud optical thicknesses and mean effective sizes was examined by comparison with MODIS cloud products. The quality of retrieved cloud top and cloud base ice crystal effective sizes was evaluated by comparison with those derived from observations by the ground-based MMCR and CPR/CloudSat. These assessments show that retrieved cloud optical thicknesses and mean effective sizes correlate well with MODIS cloud products. Retrieved mean effective sizes are also well correlated with radar-derived mean sizes, but are generally smaller in magnitude, because of the fact that radar beam tends to miss small cloud particles.

[50] Overall, the cirrus cloud vertical sizing retrieval algorithm represents a step of progress in the development of satellite cloud retrieval program in terms of its capability to determine the vertical cloud particle size profile, and is potentially applicable to the processing of remote sensing data from the next generation VIIRS/NPOESS, which is to be launched beyond 2010. Clearly, to make this algorithm operationally viable on a global scale, much more research works are needed to improve the performance of retrieval algorithm. For example, the present retrieval program makes use of the ''independent pixel approximation'' in the forward radiative transfer calculations; an approximation best applicable to stratiform clouds. Note that all three cases studied in this paper were stratiform cirrus. To adequately account for horizontal radiative transfer associated with cloud inhomogeneity, particularly in vertically convective clouds, a 3-D radiative transfer model coupled with an intricate numerical iterative retrieval scheme are required, a challenging research subject requiring further exploration and numerical study.

[51] **Acknowledgments.** This research was supported by NSF grant ATM-0331550 and by DOE grant DEFG03–00ER62904.

## References

Baum, B. A., D. P. Kratz, P. Yang, S. Ou, Y. Hu, P. F. Soulen, and S.-C. Tsay (2000), Remote sensing of cloud properties using MODIS airborne simulator imagery during SUCCESS: 1. Data and models, *J. Geophys. Res.*, *105*(D9), 11,767–11,780.

Baum, B. A., A. J. Heymsfield, P. Yang, and S. T. Bedka (2005a), Bulk scattering properties for the remote sensing of ice clouds. Part I: Microphysical data and models, *J. Appl. Meteorol.*, *44*(12), 1885–1895, doi:10.1175/JAM2308.1.

Baum, B. A., Y.-X. Hu, P. Yang, A. J. Heymsfield, S. Platnick, M. D. King, and S. T. Bedka (2005b), Bulk scattering properties for the remote sensing of ice clouds. Part II: Narrowband models, *J. Appl. Meteorol.*, *44*(12), 1896–1911, doi:10.1175/JAM2309.1.

Chang, F.-L., and Z. Li (2002), Estimating the vertical variation of cloud droplet effective radius using multispectral near-infrared satellite measurements, *J. Geophys. Res.*, *107*(D15), 4257, doi:10.1029/2001JD000766.

Comstock, J. M., T. P. Ackerman, and G. G. Mace (2002), Ground-based lidar and radar remote sensing of tropical cirrus clouds at Nauru Island: Cloud statistics and radiative impacts, *J. Geophys. Res.*, *107*(D23), 4714, doi:10.1029/2002JD002203.

Fu, Q. (1996), An accurate parameterization of the solar radiative properties of cirrus clouds for climate models, *J. Clim.*, *9*(9), 2058–2082, doi:10.1175/1520-0442(1996)009<2058:AAPOTS>2.0.CO;2.

Fu, Q., and K.-N. Liou (1993), Parameterization of the radiative properties of cirrus clouds, *J. Atmos. Sci.*, *50*(13), 2008–2025, doi:10.1175/1520-0469(1993)050<2008:POTRPO>2.0.CO;2.

Gu, Y., and K. N. Liou (2001), Radiation parameterization for three-dimensional inhomogeneous cirrus clouds: Application to climate models, *J. Clim.*, *14*(11), 2443–2457, doi:10.1175/1520-0442(2001)014<2443:RPFTDI>2.0.CO;2.

Gu, Y., and K. N. Liou (2006), Cirrus cloud horizontal and vertical inhomogeneity effects in a GCM, *Meteorol. Atmos. Phys.*, *91*, 223–235, doi:10.1007/s00703-004-0099-2.

Gu, Y., J. Farrara, K. N. Liou, and C. Mechoso (2003), Parameterization of cloud-radiation processes in the UCLA general circulation model, *J. Clim.*, *16*(20), 3357–3370, doi:10.1175/1520-0442(2003)016<3357:POCPIT>2.0.CO;2.

Heymsfield, A. J., and J. Iaquinta (2000), Cirrus crystal terminal velocities, *J. Atmos. Sci.*, *57*(7), 916–938, doi:10.1175/1520-0469(2000)057<0916:CCTV>2.0.CO;2.

King, M. D., S.-C. Tsay, S. E. Platnick, M. Wang, and K. N. Liou (1997), Cloud retrieval algorithms for MODIS: Optical thickness, effective particle radius, and thermodynamic phase, *MODIS Algorithm Theor. Basis Doc. ATBDMOD-05*, NASA Goddard Space Flight Cent., Greenbelt, Md. (Available at http://modis-atmos.gsfc.nasa.gov/_docs/atbd_mod05.pdf.)

Kinne, S., et al. (1997), Cirrus cloud radiative and microphysical properties from ground observations and in situ measurements during FIRE 1991 and their application to exhibit problems in cirrus solar radiative transfer modeling, *J. Atmos. Sci.*, *54*(18), 2320–2344, doi:10.1175/1520-0469(1997)054<2320:CCRAMP>2.0.CO;2.

Liou, K. N. (2002), *An Introduction to Atmospheric Radiation*, 2nd ed., 583 pp., Academic, Amsterdam.

Liou, K. N., S. Ou, Y. Takano, J. Roskovensky, G. Mace, K. Sassen, and M. Poellot (2002), Remote sensing of three-dimensional inhomogeneous cirrus clouds using satellite and mm-wave cloud radar data, *Geophys. Res. Lett.*, *29*(9), 1360, doi:10.1029/2002GL014846.

Liou, K. N., S.-C. Ou, Y. Takano, and J. Cetola (2006), Remote sensing of three-dimensional cirrus clouds from satellites: Application to continuous wave laser atmospheric transmission and backscattering, *Appl. Opt.*, *45*(26), 6849–6859, doi:10.1364/AO.45.006849.

Mace, G., A. Heymsfield, and M. Poellot (2002), On retrieving the microphysical properties of cirrus clouds using the moments of the millimeter-wavelength Doppler spectrum, *J. Geophys. Res.*, *107*(D24), 4815, doi:10.1029/2001JD001308.

Matrosov, S., B. Orr, R. Kropfli, and J. Snider (1994), Retrieval of vertical profiles of cirrus cloud microphysical parameters from Doppler radar and infrared radiometer measurements, *J. Appl. Meteorol.*, *33*(5), 617–626, doi:10.1175/1520-0450(1994)033<0617:ROVPOC>2.0.CO;2.

Menzel, W. P., B. A. Baum, R. A. Frey, and H. Zhang (2006), Cloud top properties and cloud phase, *MODIS Algorithm Theor. Basis Doc. ATBDMOD-06*, 61 pp., NASA Goddard Space Flight Cent., Greenbelt, Md. (Available at http://modis-atmos.gsfc.nasa.gov/_docs/MOD06CT:MYD06CT_ATBD_C005.pdf.)

Miloshevich, L. M., and A. J. Heymsfield (1997), A balloon-borne continuous cloud particle replicator for measuring vertical profiles of cloud microphysical properties: Instrument design, performance, and collection efficiency analysis, *J. Atmos. Oceanic Technol.*, *14*, 753–768, doi:10.1175/1520-0426(1997)014<0753:ABBCCP>2.0.CO;2.

Minnis, P., P. W. Heck, and D. F. Young (1993), Inference of cirrus cloud properties using satellite-observed visible and infrared radiances. Part II: Verification of theoretical cirrus radiative properties, *J. Atmos. Sci.*, *50*(9), 1305–1322, doi:10.1175/1520-0469(1993)050<1305:IOCCPU>2.0.CO;2.

Mishchenko, M. I., W. B. Rossow, A. Macke, and A. A. Lacis (1996), Sensitivity of cirrus cloud albedo, bidirectional reflectance and optical thickness retrieval accuracy to ice particle shape, *J. Geophys. Res.*, *101*(D12), 16,973–16,985.

Nakajima, T. Y., and T. Nakajima (1995), Wide-area determination of cloud microphysical properties from MOAA AVHRR measurements for FIRE and ASTEX regions, *J. Atmos. Sci.*, *52*(23), 4043–4059, doi:10.1175/1520-0469(1995)052<4043:WADOCM>2.0.CO;2.

Ou, S. C., K. N. Liou, Y. Takano, N. X. Rao, Q. Fu, A. J. Heymsfield, L. M. Miloshevich, B. Baum, and S. A. Kinne (1995), Remote sounding of cirrus cloud optical depths and ice crystal sizes from AVHRR data: Verification using FIRE II IFO measurements, *J. Atmos. Sci.*, *52*(23), 4143–4158, doi:10.1175/1520-0469(1995)052<4143:RSOCCO>2.0.CO;2.

Ou, S. C., and K. N. Liou (1995), Ice microphysics and climatic temperature feedback, *Atmos. Res.*, *35*, 127–138.

Ou, S. C., Y. Takano, K. N. Liou, G. J. Higgins, A. George, and R. Slonaker (2003), Remote sensing of cirrus cloud optical thickness and effective particle size for the national polar-orbiting operational environmental satellite system visible infrared imager radiometer suite: Sensitivity to instrument noise and uncertainties in environmental parameters, *Appl. Opt.*, *42*(36), 7202–7214, doi:10.1364/AO.42.007202.

Platnick, S. (2000), Vertical photon transport in cloud remote sensing problems, *J. Geophys. Res.*, *105*(D18), 22,919–22,935.

Platnick, S., M. King, S. Ackerman, W. Menzel, B. Baum, J. Riedi, and R. Frey (2003), The MODIS cloud products—Algorithms and examples from Terra, *IEEE Trans. Geosci. Remote Sens.*, *41*(2), 459–473, doi:10.1109/TGRS.2002.808301.

Sassen, K. (1991), Corona-producing cirrus cloud properties derived from polarization lidar and photographic analyses, *Appl. Opt.*, *30*, 3421–3428, doi:10.1364/AO.30.003421.

Spinhirne, J. D., and W. D. Hart (1990), Cirrus structure and radiative parameters from airborne lidar and spectral radiometer observations: The 28 October 1986 FIRE study, *Mon. Weather Rev.*, *118*(11), 2329–2343, doi:10.1175/1520-0493(1990)118<2329:CSARPF>2.0.CO;2.

Wang, M., and M. D. King (1997), Correction of Rayleigh scattering effects in cloud optical thickness retrievals, *J. Geophys. Res.*, *102*(D22), 25,915–25,926.

Wong, E., K. Hutchison, S. C. Ou, and K. N. Liou (2007), Cirrus cloud top temperatures retrieved from radiances in the National Polar-Orbiting Operational Environmental Satellite System—Visible Infrared Imager Radiometer Suite 8.55 and 12.0 $\mu$m band passes, *Appl. Opt.*, *46*, 1316–1325, doi:10.1364/AO.46.001316.

Yang, P., K. N. Liou, K. Wyser, and D. Mitchel (2000), Parameterization of the scattering and absorption properties of individual ice crystals, *J. Geophys. Res.*, *105*, 4699–4718, doi:10.1029/1999JD900755.

Yue, Q., K. N. Liou, S. C. Ou, B. H. Kahn, P. Yang, and G. G. Mace (2007), Interpretation of AIRS data in thin cirrus atmospheres based on a fast radiative transfer model, *J. Atmos. Sci.*, *64*, 3827–3842, doi:10.1175/2007JAS2043.1.

M. Deng, Department of Atmospheric Science, University of Wyoming, Department 3038, 1000 East University Avenue, Laramie, WY 82071, USA.

K. N. Liou, S. S. C. Ou, and X. Wang, Department of Atmospheric and Oceanic Sciences, University of California, Los Angeles, 7127 Math Sciences Building, 405 Hilgard Avenue, Los Angeles, CA 90095, USA. (ssou@atmos.ucla.edu)

G. G. Mace, Department of Meteorology, University of Utah, Room 819, 135 South 1460 East, Salt Lake City, UT 84112-0110, USA.